

ERROR ANALYSIS OF A GRAVURE PRINTING SYSTEM

PRECISION MANUFACTURING PROJECT



Alejandro de la Fuente

Wei Li

Koo-Hyun Nam

Adarsh Krishnamurthy

INDEX

Introduction.....	3
Alignment Process and Sources of Error.....	4
Experimental Position Repeatability and Alignment Accuracy.....	7
Kinematic Clamp Repeatability.....	7
Base Plate Repeatability.....	7
Print Alignment Errors.....	8
Coupled Thermal Structural Analysis.....	10
Thermal Analysis.....	11
Structural Analysis.....	12
HTM Analysis.....	14
Components.....	14
HTMs for Camera 1.....	15
HTMs for Camera 2.....	17
HTMs for camera 3.....	18
Calculated Error Components.....	19
Worst Case Error Estimation.....	20
Error Budget.....	21
Discussion.....	21
Conclusion.....	22

INTRODUCTION

Printing presses have had an enormous impact on our ability to share and communicate ideas, ever since Gutenberg's first inventions. Today, the vast majority of print material is produced on roll-type printing presses using a variety of techniques including lithography, offset printing, flexography and gravure. Of these techniques, gravure is the least complex, and offers the highest resolution. This has made it an attractive candidate for use in manufacturing printed electronics, where resolution requirements are much higher than those required for publication prints. Using a high throughput process to manufacture integrated circuits has the potential of providing ultra low cost electronics that can have a vast number of new applications, such as electronic paper, smart labels and embedded sensors. All of which aim at providing us with a higher quality of life.

The field of printed electronics is still in development, and thus, the majority of printing work is done at a laboratory level, most commonly with ink-jet printers that provide enormous flexibility and small material volume requirements. However, ink-jet is not a technology that can easily provide for high volume manufacturing, and inks developed for ink-jet do not easily transfer to high volume roll-type processes. Thus a small, bench top gravure printing system was developed (Figure 1) which has a small printing form, requiring a small amount of printing material, and has the ability to do high accuracy registration, making fine-line, multilayer prints possible.

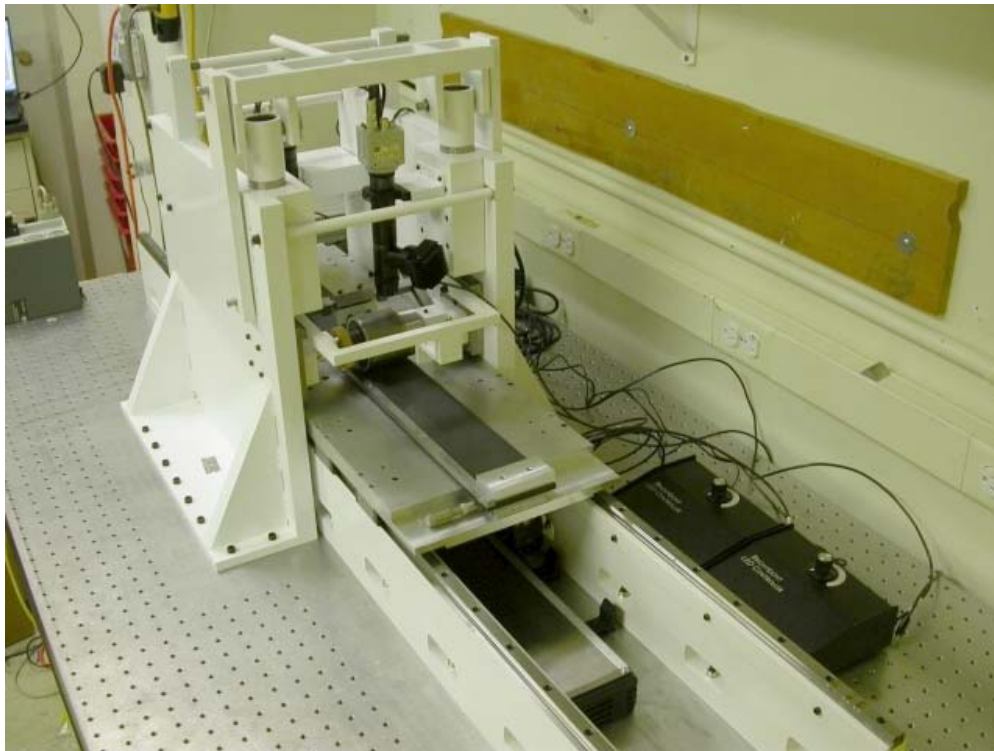


Figure 1: A bench top, sheet-fed, high-resolution gravure printing system with a 5cm printing form.

The goal of this paper is to describe and analyze the registration capability of this printing machine, in order to determine the major sources of alignment error, and determine possible solutions to these errors. A description of the alignment process will be given followed by an experimental determination of its printing errors. With this in mind, we take on the task of determining the sources of error using homogeneous transformation matrices (HTMs). We first determine the thermal errors from a coupled thermal-structural analysis of the machine using finite element simulations, then we combine these errors with errors coming from a variety of other sources such as the motors and stages which move the machine components during a print, and we calculate the total expected alignment error using HTMs. Finally, we propose a series of improvements to the printing system, using the knowledge gleaned from our analysis.

ALIGNMENT PROCESS AND SOURCES OF ERROR

The gravure printing system shown in Figure 1 is a sheet fed system that operates as follows: A plastic sheet (a.k.a. substrate) is mounted on the black sample holder with a rubber backing using two clamps. The sample holder is then mounted onto a larger base plate (a.k.a. top plate) and two high precision double-row ball bearing Newport stages through a kinematic clamp. The substrate is then aligned to the gravure roll using three Navitar microscopes, a small piece of alignment software, the aforementioned Newport stages to provide motion in the y and theta directions, as well as a Parker-Hafnlin linear motor which moves the stage in the printing direction x. Once the alignment has been done with the roll sitting slightly above the substrate, it is lowered onto the substrate and loaded with a spring-based compression system to a weight of approximately 10kg and the alignment is re-checked. If the alignment is good, a doctor blade is placed against the roll, the roll is inked, then the substrate is moved under the roll (which rotates) using the Parker linear motor to transfer the ink from the roll to the substrate.

The alignment routine can be described using Figure 2. The substrate is placed under the roll such that the alignment marks on the substrate are a distance x away from the axis of the roll. This distance should be 1.5 times the circumference of the roll, or $3/2\pi d$, where d is the diameter of the roll. This will ensure that the alignment mark, which is seen at the top of the roll through the roll camera, will roll directly on top of the alignment marks shown in substrate camera 1. A second alignment mark on the roll will print over the mark shown in camera 2, as long as the relative rotation of the substrate is adjusted by properly relating alignment marks on substrate camera 1 to substrate camera 2. Thus, the distance between the substrate cameras and the roll camera must also be 1.5 times the circumference of the roll to ensure the alignment marks are centered exactly in the camera window. However, since the diameter of each roll is slightly different there is a deviation of roll diameter Δd , which leads to a need to offset the alignment marks by a distance $\Delta x = 3/2\pi\Delta d$. The pattern on the roll may also not be aligned exactly in y and theta direction between roll and roll. We thus use a software program to keep calibrated values of Δd and theta, and thus corresponding values of Δx and Δy required to align a variety of different rolls to each other.

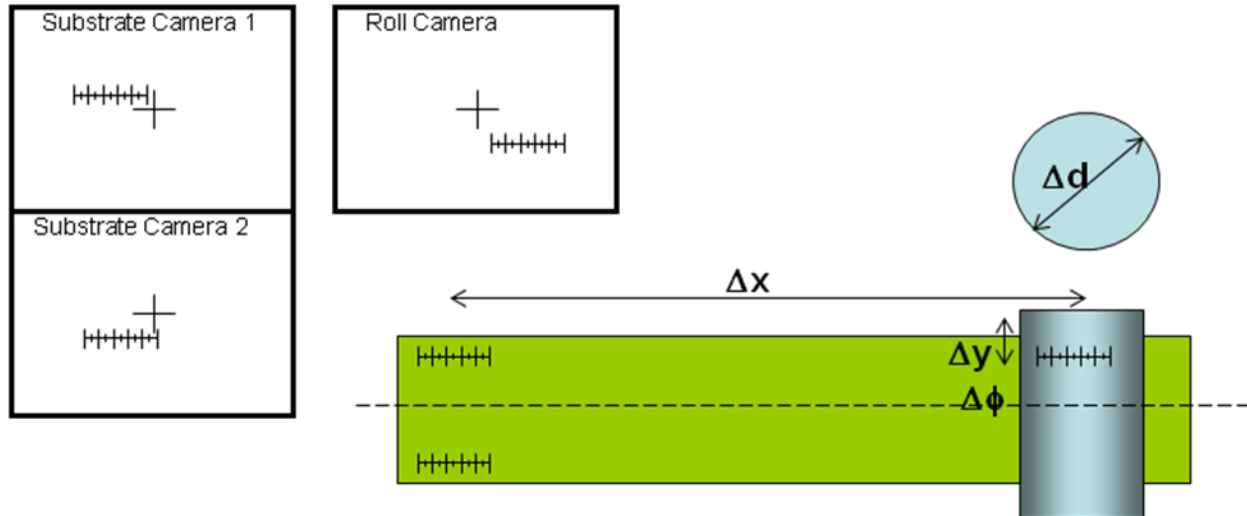


Figure 2: Diagram of the alignment routine. Three cameras are used to align the substrate to the printing roll. The cameras are spaced such that when the alignment mark is both visible on the roll camera, as well as the substrate cameras, with appropriate spacing. The micrograph shows an example of a printed alignment mark.

The alignment system is however, susceptible to a wide variety of other errors, including but not limited to the following.

- Thermal expansion of the system as the laboratory or local machine temperatures change with time, and use.
- The relative position of the cameras affected by either mechanical disturbances, or thermal expansion.
- The actual position with which the roll is mounted in the machine, since we assume in our alignment routine that the roll positioned in the exact position every time, and more specifically that theta errors come only from the theta offset of the patten on the roll, and not the roll position itself.
- The ability of the kinematic clamp to hold the substrate holder in place, without it moving during the print.
- Deformations of the flexible substrate, and rubber backing during the printing process, which may lead to stretching of the printed pattern and slip between roll and substrate.
- Stiffness and position control of the Newport stages, which are used to move the substrate in y and theta directions, as well as the stiffness and position control of the Newport stages that move the roll up and down into printing position.
- Stiffness and straightness of the Parker linear motor that moves the substrate during the print.
- The movement of the roll caused by the pressure of the doctor blade.
- Effects of the alignment procedure, and printing process, including care of handling components, order in which parts are assembled and particulars of the alignment sequence.

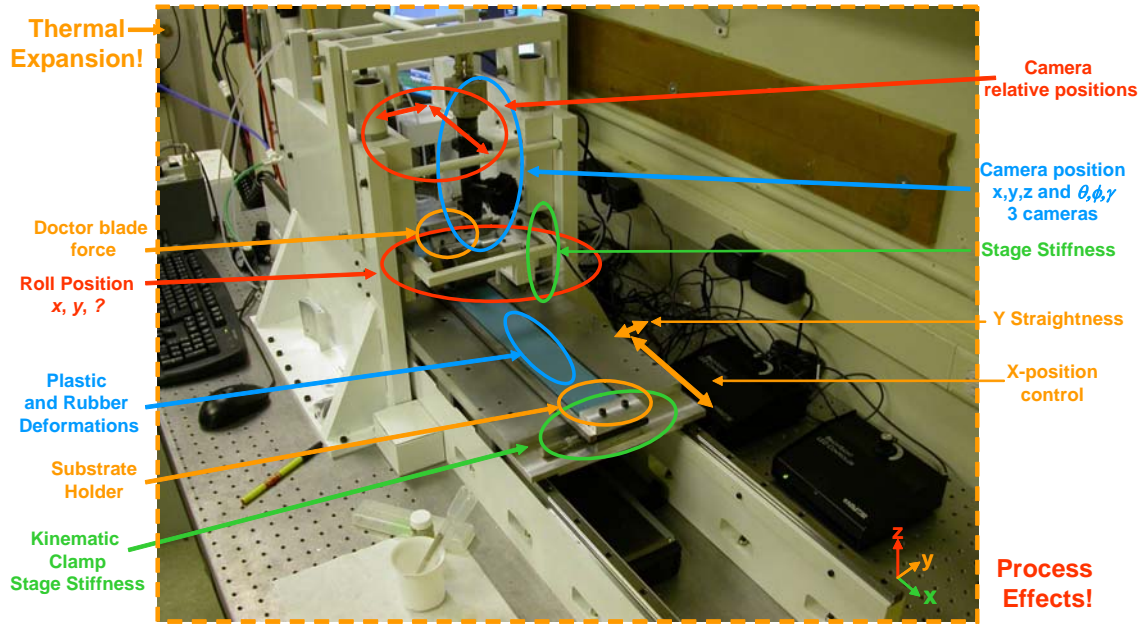


Figure 3: Gravure printing system and a range of possible sources of error.

It is clear that modeling every source of error would be a difficult undertaking. Thus in order to reduce the complexity and make our calculations tractable, we selected what we believed to be the prominent sources of error and made a computer model of the printing system that can then be later used with appropriate finite element programs to model the total system error. The main sources of errors and computer generated system model are shown in Figure 3. We selected thermal errors, camera positions, repeatability of the kinematic clamp and position accuracy of the substrate in x and y directions as our preliminary investigations led us to believe these are errors which large possible deviations on the order of microns or more.

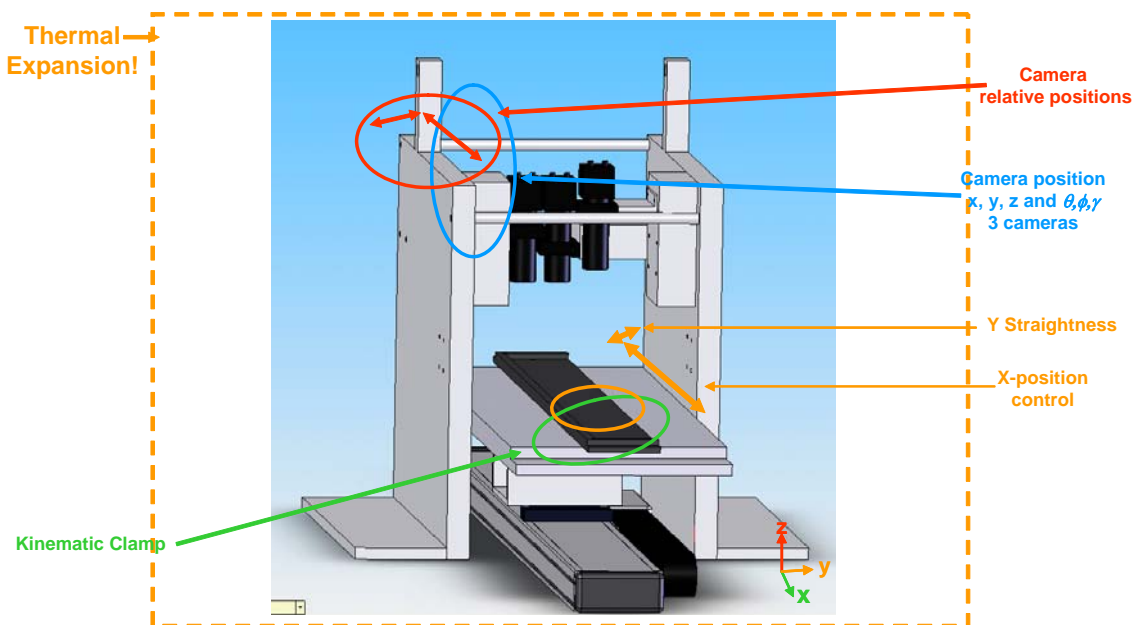


Figure 4: Computer model of gravure printing system and predicted major sources of error.

EXPERIMENTAL POSITION REPEATABILITY AND ALIGNMENT ACCURACY

As built, this gravure printing system was intended to afford up to $5\mu\text{m}$ alignment accuracy. However, we quickly determined that the practical alignment accuracy of the machine was, in fact, much worse. In order to isolate the major sources of error a few repeatability experiments were carried out on the machine. Using an electronic Mitutoyo indicator with a $1\mu\text{m}$ resolution, we quickly assessed that a major source of error came from positional repeatability of the substrate. This could be due to the repeatability of the kinematic clamp, which was designed to couple the substrate holder to the Newport stages on the base plate, while still affording movement of the substrate holder in y and theta directions. It could also be due to the repeatability of the parker stage, which should move the substrate straight under the roller and back to the same position after the print.

KINEMATIC CLAMP REPEATABILITY

In order to assess the repeatability of the kinematic clamp, the substrate was placed on the base plate and clamp, and its position in the x and y direction was measured with the electronic indicator. The substrate holder was then removed and the process repeated 50 times, taking measurements in x and y at both extremes of the substrate holder, centered about the contact point of each kinematic clamp (one at the front of the substrate holder, and one at the back). The data collected is presented in Figure 5. Clearly, repeatability for both clamps is worse than $5\mu\text{m}$, especially in the y direction where the error is $\pm 30\mu\text{m}$ for the front clamp and $\pm 20\mu\text{m}$ for the back clamp.

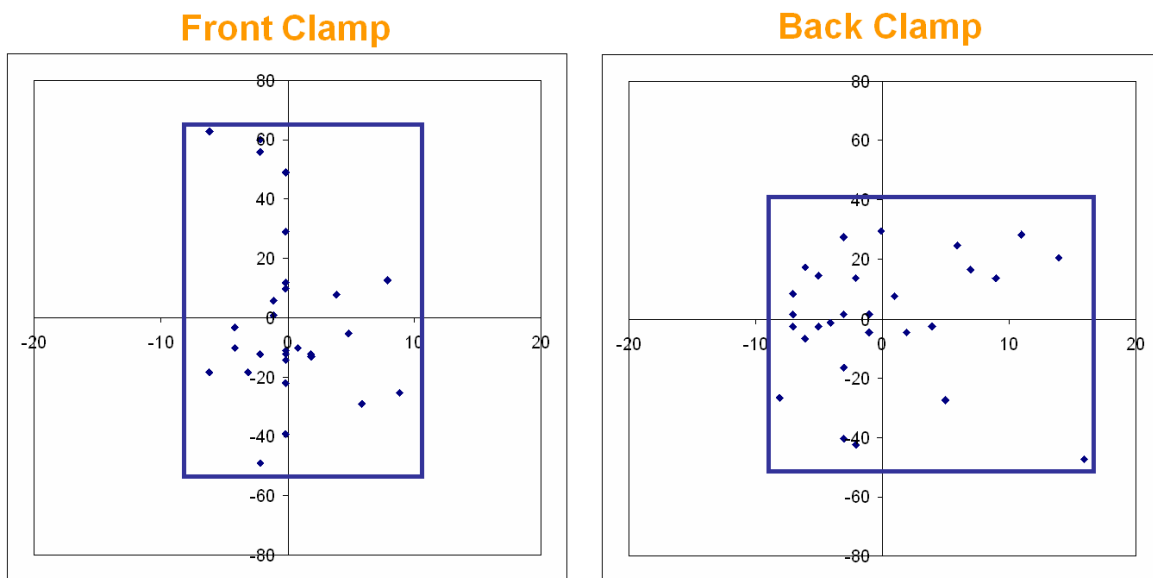


Figure 5: Position repeatability of substrate holder kinematic clamps. For the front clamp $\Delta x = \pm 5\mu\text{m}$, $\Delta y = \pm 30\mu\text{m}$, for the back clamp $\Delta x = \pm 7\mu\text{m}$, $\Delta y = \pm 20\mu\text{m}$.

BASE PLATE REPEATABILITY

We also tested the repeatability of the base plate (onto which the substrate holder is placed) and parker motor using a similar technique. We mounted a small photo-lithographically patterned silicon wafer onto the sample holder using a double sided 3M brand tape, and moved

the stage back and forth 500mm 50 times measuring the position of a small alignment mark on the wafer, in the field of view of the camera.

The resolution of the camera was calibrated to be $0.62\mu\text{m}/\text{pixel}$ with an 860×640 pixel display. We used an onscreen cursor with a pixel position-tracking program to align a crosshair cursor to the center of a crosshair alignment mark that was patterned onto the wafer with a $5\mu\text{m}$ line width. This allowed for easy centering as the eye can easily catch the symmetry of light shining on the dark cursor crosshair from the shiny gold alignment mark.

Surprisingly, after measuring the position of the crosshair after 500mm back-and-forth movements using a velocity of 20cm/s and an acceleration of 40 m/s^2 , we found that the positional error was only $\pm 0.36\mu\text{m}$ in the y-direction (perpendicular to the direction of motion) and $\pm 1.63\mu\text{m}$ along the x-direction, the direction of motion. The two graphs presented below indicate that there is indeed more control in the y direction than in the x (Figure 6) but even more importantly, there seems to be a systematic deviation in x-position as the number of measurements progresses. This is presumably because the encoder on the Parker stage may miss a measurement at some common interval. This systematic deviation was only seen for high-speed motions of 20 cm/s .

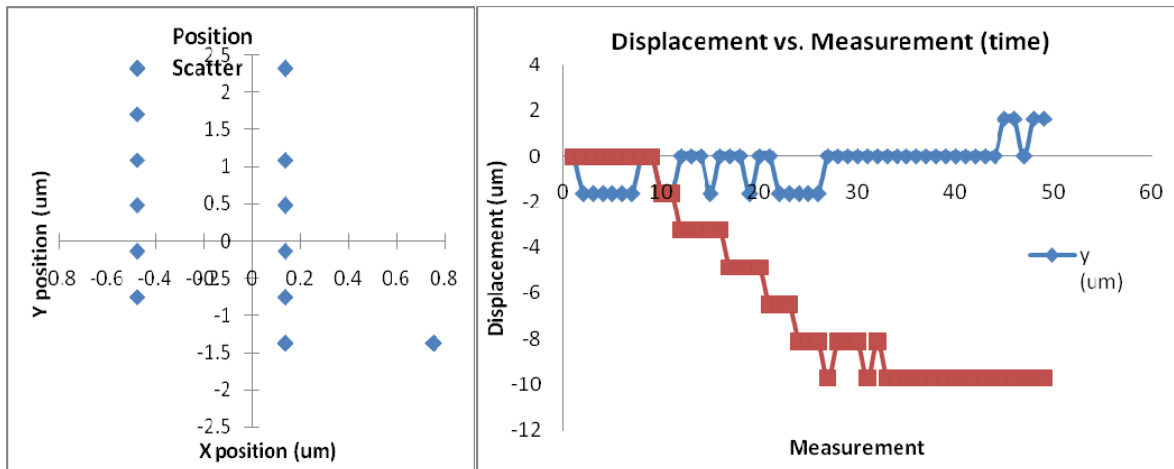


Figure 6: Scatter plot of x and y repeatability of base plate position (left), and x and y position vs. time (right). It can be seen that the machine shows only a small amount of creep over time.

PRINT ALIGNMENT ERRORS

If errors in the substrate position were the only sources of error, summing the errors from the kinematic clamp and base plate positions alone would give a total error shown in equation (1) and (2) where ε_x , and ε_y are the standard deviations of the position.

$$\varepsilon_x = \sqrt{\varepsilon_{x-clamp}^2 + \varepsilon_{x-base}^2} = 3.99\mu\text{m} \quad (1)$$

$$\varepsilon_y = \sqrt{\varepsilon_{y-clamp}^2 + \varepsilon_{y-base}^2} = 28.63\mu\text{m} \quad (2)$$

However, in practice the error is still much greater than this. We made a series of eight prints using two types of gravure inks. One conductive carbon ink (DuPont 5069) and one silver flake ink (DuPont 5067). The carbon conductive ink was printed on 8 blank polyester substrates (DuPont Melinex ST505), and left to dry over night. After drying, the substrates were aligned to the same roll used to print the carbon ink using the alignment procedure described above and a silver ink was printed. The use of these two inks provided good contrast between the reflective silver ink and the black carbon ink so that alignment errors can be easily detected in an optical microscope as shown in Figure 7. Unfortunately, the alignment errors were on the order of 50 to 150 μm as shown in Figure 8. Larger values of misalignment were measured on the right alignment mark, which may be a result of the fact that the shape of the alignment mark on the right is different from that on the left, which may provide with a better reference with which to measure the alignment error.

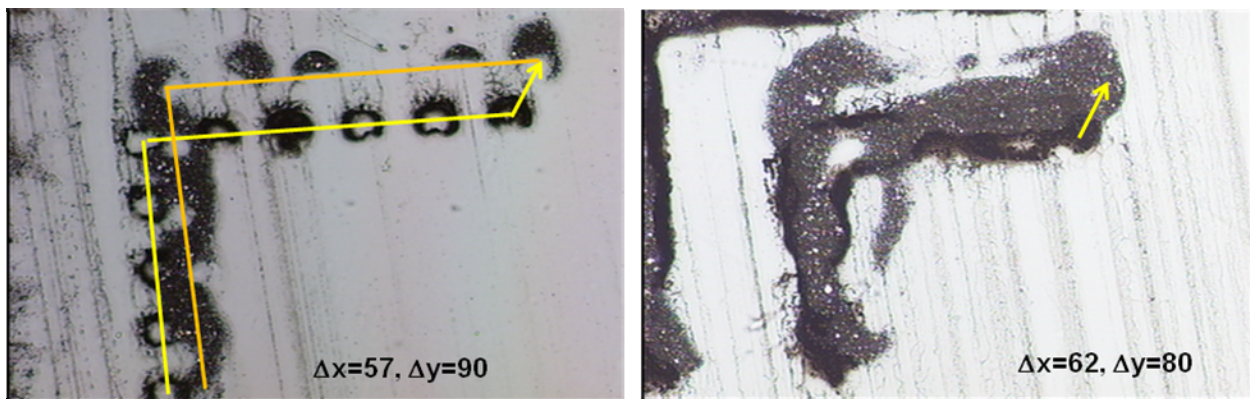


Figure 7: Results of a two-layer print with carbon conductive ink as the bottom layer and silver conductive ink as the top layer. The orange and yellow lines on the left image help distinguish the two alignment marks of interest.

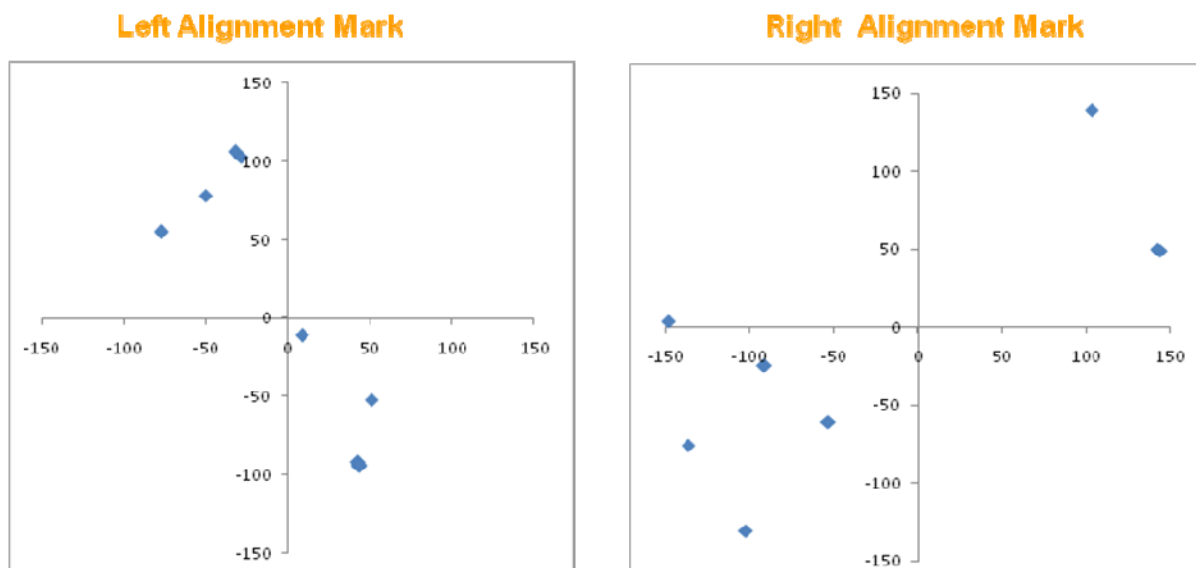


Figure 8: Scatter plot of alignment errors for 8 different two-layer prints. The left plot shows alignment errors measured on the left alignment mark and the right plot shows errors measured on the right alignment mark. It should be noted that the shape of the alignment mark itself could lead to measurement errors.

It is thus clear that not only does the stage position contribute a considerable component of misalignment but also there are other components that also contribute to the error. We thus proceed to analyze other sources of error in the machine using finite element modeling and homogeneous transfer matrices.

COUPLED THERMAL STRUCTURAL ANALYSIS

From the previous section, it was found experimentally that the printing system had an alignment error on the order of $100\mu\text{m}$. To understand the source of this error, a coupled thermal-structural analysis was performed on the optical alignment system and the results of this analysis were further used for a HTM analysis.

Figure 9 shows the steps for the coupled analysis. However, it is not exactly accurate, as the deformed structure is not used for the thermal analysis. The main steps in the process are to mesh the imported model and perform a thermal analysis using the unreformed model. Then the temperature values obtained from the thermal analysis is then used for a structural analysis where the thermal deformations are taken into account by the finite element model.

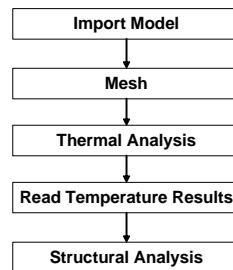


Figure 9: Steps in coupled thermal structural analysis

We used the commercially available package SolidWorks for modeling the whole system. Then this model was imported into ANSYS, a commercial finite element modeling package. Figure 10 shows the structural model that was used for the coupled analysis. The model could have been made simpler by not including the screw holes, as it would have made the meshing easier. Nevertheless, since there were many screw holes, they might significantly affect the temperature distribution and the displacements. Hence, the complete model was used for the analysis.

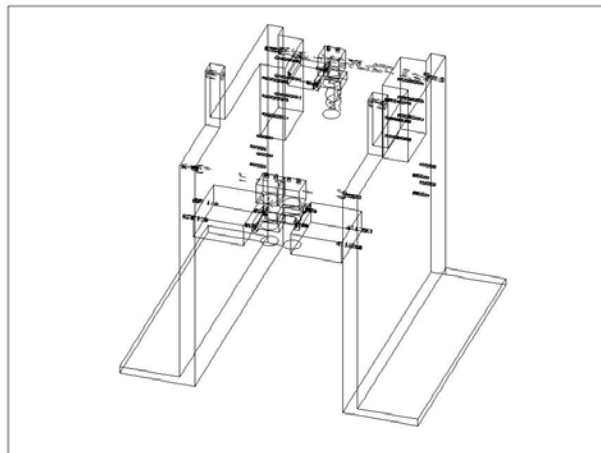


Figure 10: Structural model of the optical camera alignment system

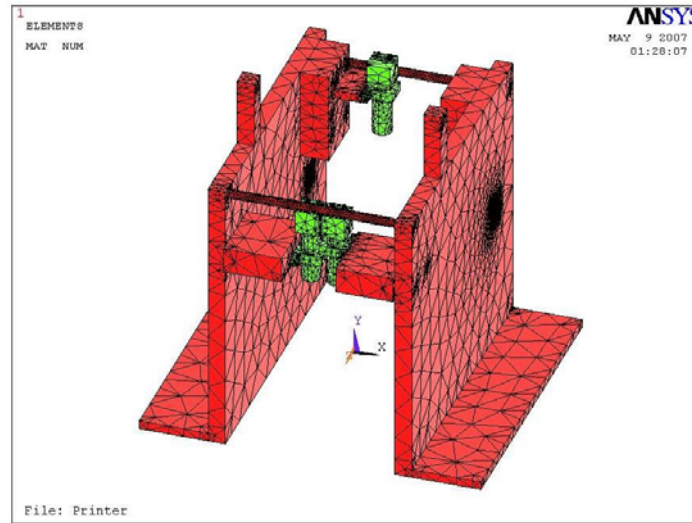


Figure 11: Complete model after meshing. Green elements are made of Aluminum and the red elements are made of Steel.

The model was then meshed in ANSYS as shown in Figure 11. Since finite element analyses have to be verified for mesh independence, the model was meshed in three different ways using different number and type of elements. The details of the three different cases are given in Table 1. The 20-Node Brick element is a second order element and has nodes on the mid-edges of the elements to improve the accuracy of the calculations. Finally, since the model was made of both Aluminum and Steel, the correct material properties were given to the corresponding elements.

Table 1: Details of the different FE cases

	Case 1	Case 2	Case 3
Element Type	8-Node Brick	8-Node Brick	20-Node Brick
No. of Nodes	61486	63128	424483
No. of Elements	300234	313473	286927

THERMAL ANALYSIS

As explained above, the model was meshed in three different ways and the thermal analysis was performed on each of the cases. A temperature difference of 5°C was assumed between the base and the top of the model. Since the printer was not located in a temperature-controlled environment, this temperature difference is reasonable. The printer is mounted on a solid base and hence the base is assumed to be at a constant temperature of 300K and the top of the printer was fixed to 305K. The steady state temperature distribution is then solved for the points on the printer.

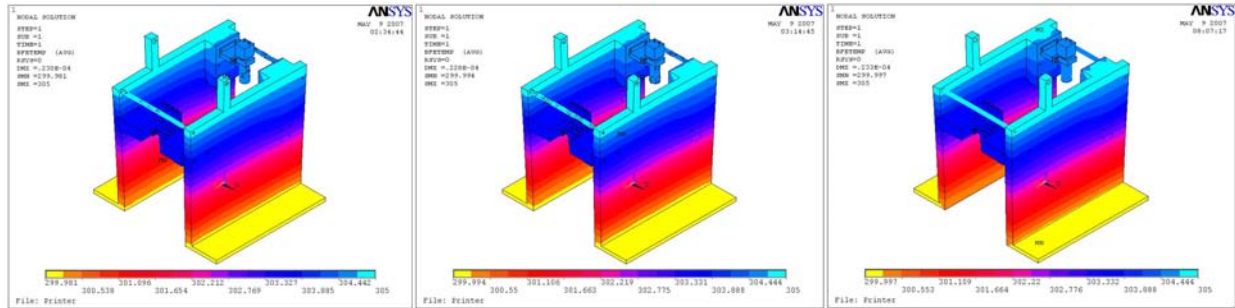


Figure 12: Plots of temperature of the structure from the thermal analysis for the three different cases. The results are almost identical for all the three cases.

Figure 12 shows the resulting temperature distribution for the three different cases. It was clear that the difference between the temperatures in the three cases is negligible and was smaller than the nominal values by several orders of magnitude.

STRUCTURAL ANALYSIS

After the thermal analysis was performed, the temperature results were used to perform a structural analysis for all the three cases. The base of the printer was fixed in all three directions as it was firmly bolted to the worktable. The temperature difference between the different parts make the structure deform or warp in different direction.

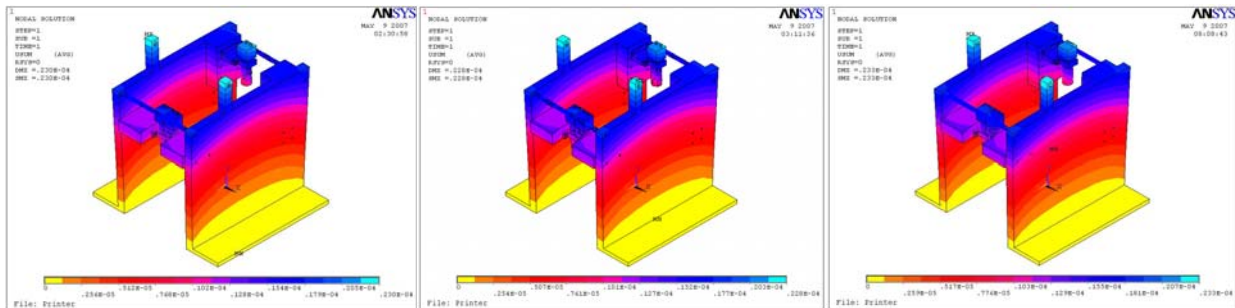


Figure 13: Plots of total displacement of the structure due to thermal effects for the three cases.

Figure 13 shows the contour plots of the resultant displacement of the structure for the three different cases. It can be seen that the deformation is zero at the base as it is fixed and it slowly increases towards the top part of the printer. Also similar to the thermal analysis, the difference in displacements between the three different cases is very small and it shows that the analysis is independent of the meshing or the elements in the finite element analysis.

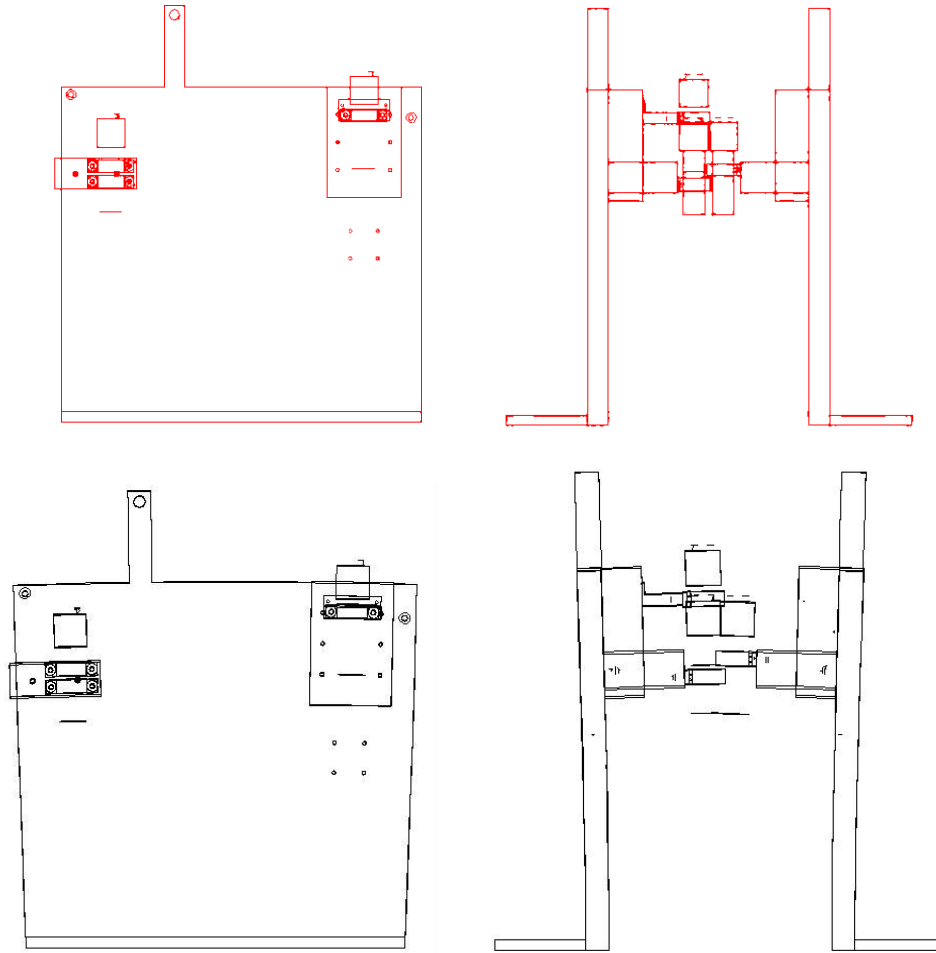


Figure 14: Original and deformed shapes of the structure. Note that the displacements in the deformed structure are scaled by a large value to enhance the deformations

Figure 14 shows the original and deformed shapes of the printer due to thermal effects. The displacements in the deformed structure are scaled to emphasize the deformations. However, it can be seen that the cameras not only shift in their position due to thermal effects but also are tilted in the process. This tilt gives rise to high error as the angle is amplified by the distance of the camera from the substrate.

In summary, the thermal errors were found to be significant in the structure even for a moderate 5°C temperature change. The errors due to camera positions on the substrate were found to be approximately $20\text{-}40\mu\text{m}$. These values were then used for the HTM analysis as explained below.

HTM ANALYSIS

The output from the coupled thermal-structural finite element analysis was used to perform an HTM analysis of the printing system. The following section gives the details of the different components of the HTM analysis as well as the theoretical error values computed from the analysis.

COMPONENTS

There are three cameras in the printer system, and for each of them we have a HTM system to analyze its alignment error. In the following section, we discuss the details of the HTMs for one camera alone, as the HTMs for the other two cameras are almost the same. However, the HTM for the third camera that looks at the roll has one more component in its structural loop (the roll).

The main components of the analysis as shown in Figure 1 are a Parker-Hafnlin linear motor with a $1\mu\text{m}$ encoder resolution (1), which is attached with a mounting place (3) via the motor carriage (2). The mounting plate drives horizontally the 25.4mm aluminum top plate (4), onto which a substrate holder (5) is fixed via a kinematic clamp. A 1mm thick rubber layer (6) is attached to the top of substrate holder. The sample (7) is then loaded on the rubber layer. The position of the sample is adjusted using the micrometer stage and the linear motor by monitoring the sample position through the camera (10), which is attached to a steel vertical column (8) through a steel camera holder (9).

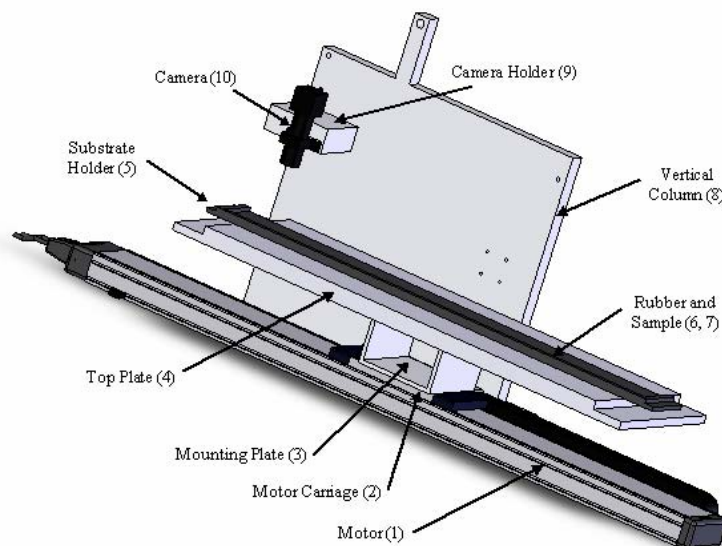


Figure 15: Components of the printer system

The actual system is considerably more complicated, but it is assumed that these components do not interfere with the positional accuracy of the stage and the positional accuracy of the sample in the stage reference and the camera reference. For example, the printer has a second set of bearings that are designed to take the vertical load from a roller, which presses

down onto the sample, in the z-direction. Since we are concerned only with x and y displacements for this analysis these components are orthogonal, and thus do not interfere. The structural loop for this camera is shown in Figure 16.

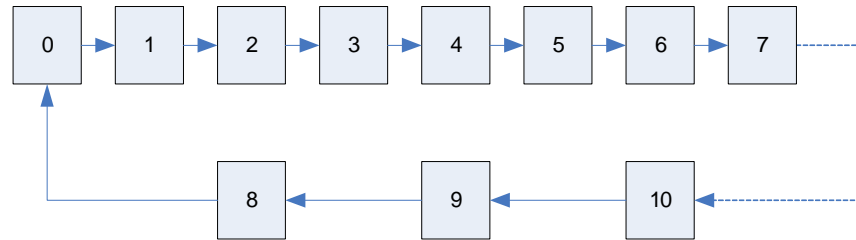


Figure 16: Structural loop for a single camera.

Figure 17 schematically shows the coordinate system and the origins (reference points) for each component in the structural loop.

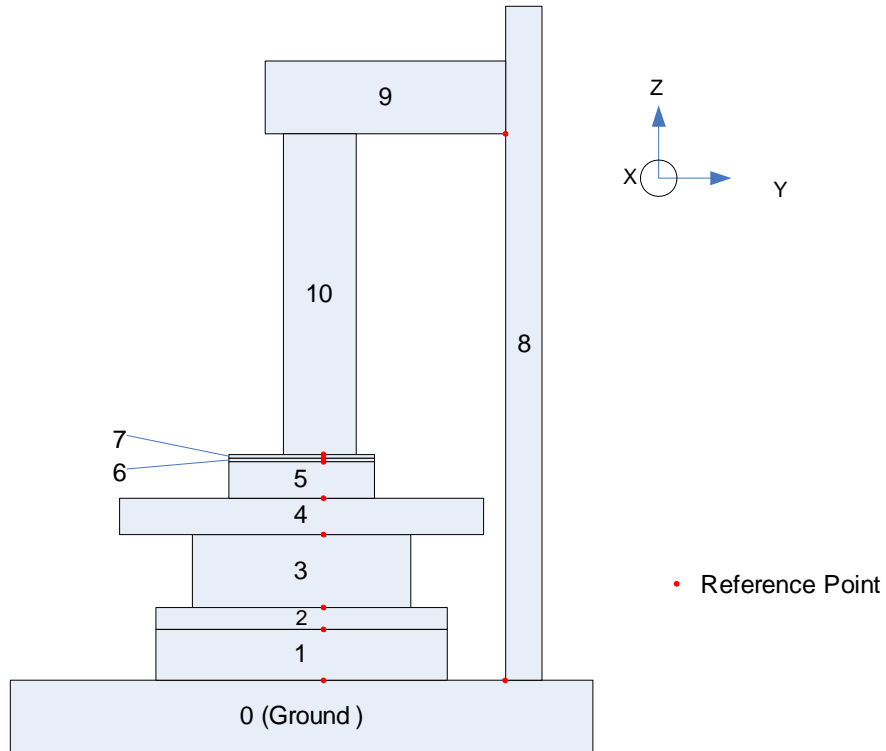


Figure 17: Coordinate systems and reference points.

HTMS FOR CAMERA 1

The systematic analysis of the alignment errors for camera 1 is listed in Table 2. The values of motion, offset and positional errors caused by thermal expansion are also specified in the table. The values of other errors are calculated in the next section.

Table 2: Analysis of alignment errors for camera 1

Component	Motion	Offset	Positional error	Roll/Pitch/Yaw
0→1		Z_1 (44.65mm)		
1→2	x (314.17mm)	Z_2 (15.35mm)	δ_{x2}	Yaw: ε_{z2}
2→3		Z_3 (76.2mm)		
3→4		Z_4 (25.4mm)		
4→5		Z_5 (6.35mm)		Yaw: ε_{z5}
5→6		Z_6 (1mm)	δ_{z6}	
6→7		Z_7 (0.5mm)	$\delta_{x7}, \delta_{y7}, \delta_{z7}$	Yaw: ε_{z7}
0→8		Y_8 (106mm)		
8→9		Z_9 (291.48mm)	δ_{x9} (-7.78 μm) δ_{y9} (3.68 μm) δ_{z9} (5.21 μm) (due to thermal expansions)	
9→10		Y_{10} (-106mm) Z_{10} (-122.03mm)	δ_{x10} (0.92 μm) δ_{y10} (-3.71 μm) δ_{z10} (2.44 μm) (due to thermal expansions)	Yaw: ε_{x10} (-89.6 μrad) Yaw: ε_{y10} (-20.3 μrad)

Based on this table, we can get the HTMs for camera 1 as below.

$$\begin{aligned}
{}^0T_1 &= \begin{pmatrix} 1 & 0 & 0 & 0 \\ 0 & 1 & 0 & 0 \\ 0 & 0 & 1 & Z_1 \\ 0 & 0 & 0 & 1 \end{pmatrix} & {}^1T_2 &= \begin{pmatrix} 1 & -\varepsilon_{z2} & 0 & x + \delta_{x2} \\ \varepsilon_{z2} & 1 & 0 & 0 \\ 0 & 0 & 1 & Z_2 \\ 0 & 0 & 0 & 1 \end{pmatrix} \\
{}^2T_3 &= \begin{pmatrix} 1 & 0 & 0 & 0 \\ 0 & 1 & 0 & 0 \\ 0 & 0 & 1 & Z_3 \\ 0 & 0 & 0 & 1 \end{pmatrix} & {}^3T_4 &= \begin{pmatrix} 1 & 0 & 0 & 0 \\ 0 & 1 & 0 & 0 \\ 0 & 0 & 1 & Z_4 \\ 0 & 0 & 0 & 1 \end{pmatrix} \\
{}^4T_5 &= \begin{pmatrix} 1 & -\varepsilon_{z5} & 0 & 0 \\ \varepsilon_{z5} & 1 & 0 & 0 \\ 0 & 0 & 1 & Z_5 \\ 0 & 0 & 0 & 1 \end{pmatrix} & {}^5T_6 &= \begin{pmatrix} 1 & 0 & 0 & 0 \\ 0 & 1 & 0 & 0 \\ 0 & 0 & 1 & Z_6 + \delta_{z6} \\ 0 & 0 & 0 & 1 \end{pmatrix} \\
{}^6T_7 &= \begin{pmatrix} 1 & -\varepsilon_{z7} & 0 & \delta_{x7} \\ \varepsilon_{z7} & 1 & 0 & \delta_{y7} \\ 0 & 0 & 1 & Z_7 + \delta_{z7} \\ 0 & 0 & 0 & 1 \end{pmatrix} & {}^0T_8 &= \begin{pmatrix} 1 & 0 & 0 & 0 \\ 0 & 1 & 0 & Y_8 \\ 0 & 0 & 1 & 0 \\ 0 & 0 & 0 & 1 \end{pmatrix} \\
{}^8T_9 &= \begin{pmatrix} 1 & 0 & 0 & \delta_{x9} \\ 0 & 1 & 0 & \delta_{y9} \\ 0 & 0 & 1 & Z_9 + \delta_{z9} \\ 0 & 0 & 0 & 1 \end{pmatrix} & {}^9T_{10} &= \begin{pmatrix} 1 & 0 & \varepsilon_{y10} & \delta_{x10} \\ 0 & 1 & -\varepsilon_{x10} & Y_{10} + \delta_{y10} \\ -\varepsilon_{y10} & \varepsilon_{x10} & 1 & Z_{10} + \delta_{z10} \\ 0 & 0 & 0 & 1 \end{pmatrix}
\end{aligned}$$

HTMS FOR CAMERA 2

The HTM analysis for camera 2 is almost the same as that for camera 1, except that the camera height and the thermal expansion are different since the two camera systems are not symmetric.

Table 3: Analysis of alignment errors for camera 2

Component	Motion	Offset	Positional error	Roll/Pitch/Yaw
0→1		Z_1 (44.65mm)		
1→2	x (314.17mm)	Z_2 (15.35mm)	δ_{x2}	Yaw: ε_{z2}
2→3		Z_3 (76.2mm)		
3→4		Z_4 (25.4mm)		
4→5		Z_5 (6.35mm)		Yaw: ε_{z5}
5→6		Z_6 (1mm)	δ_{z6}	
6→7		Z_7 (0.5mm)	$\delta_{x7}, \delta_{y7}, \delta_{z7}$	Yaw: ε_{z7}
0→8		Y_8 (-106mm)		
8→9		Z_9 (310.53mm)	δ_{x9} (-6.91 μm) δ_{y9} (-3.80 μm) δ_{z9} (5.74 μm) (due to thermal expansions)	
9→10		Y_{10} (106mm) Z_{10} (-141.08mm)	δ_{x10} (-0.27 μm) δ_{y10} (3.28 μm) δ_{z10} (2.99 μm) (due to thermal expansions)	Yaw: ε_{x10} (-60.6 μrad) Yaw: ε_{y10} (-19.7 μrad)

$$\begin{aligned}
 {}^0T_1 &= \begin{pmatrix} 1 & 0 & 0 & 0 \\ 0 & 1 & 0 & 0 \\ 0 & 0 & 1 & Z_1 \\ 0 & 0 & 0 & 1 \end{pmatrix} & {}^1T_2 &= \begin{pmatrix} 1 & -\varepsilon_{z2} & 0 & x + \delta_{x2} \\ \varepsilon_{z2} & 1 & 0 & 0 \\ 0 & 0 & 1 & Z_2 \\ 0 & 0 & 0 & 1 \end{pmatrix} \\
 {}^2T_3 &= \begin{pmatrix} 1 & 0 & 0 & 0 \\ 0 & 1 & 0 & 0 \\ 0 & 0 & 1 & Z_3 \\ 0 & 0 & 0 & 1 \end{pmatrix} & {}^3T_4 &= \begin{pmatrix} 1 & 0 & 0 & 0 \\ 0 & 1 & 0 & 0 \\ 0 & 0 & 1 & Z_4 \\ 0 & 0 & 0 & 1 \end{pmatrix} \\
 {}^4T_5 &= \begin{pmatrix} 1 & -\varepsilon_{z5} & 0 & 0 \\ \varepsilon_{z5} & 1 & 0 & 0 \\ 0 & 0 & 1 & Z_5 \\ 0 & 0 & 0 & 1 \end{pmatrix} & {}^5T_6 &= \begin{pmatrix} 1 & 0 & 0 & 0 \\ 0 & 1 & 0 & 0 \\ 0 & 0 & 1 & Z_6 + \delta_{z6} \\ 0 & 0 & 0 & 1 \end{pmatrix} \\
 {}^6T_7 &= \begin{pmatrix} 1 & -\varepsilon_{z7} & 0 & \delta_{x7} \\ \varepsilon_{z7} & 1 & 0 & \delta_{y7} \\ 0 & 0 & 1 & Z_7 + \delta_{z7} \\ 0 & 0 & 0 & 1 \end{pmatrix} & {}^0T_8 &= \begin{pmatrix} 1 & 0 & 0 & 0 \\ 0 & 1 & 0 & Y_8 \\ 0 & 0 & 1 & 0 \\ 0 & 0 & 0 & 1 \end{pmatrix}
 \end{aligned}$$

$${}^8T_9 = \begin{pmatrix} 1 & 0 & 0 & \delta_{x9} \\ 0 & 1 & 0 & \delta_{y9} \\ 0 & 0 & 1 & Z_9 + \delta_{z9} \\ 0 & 0 & 0 & 1 \end{pmatrix} \quad {}^9T_{10} = \begin{pmatrix} 1 & 0 & \varepsilon_{y10} & \delta_{x10} \\ 0 & 1 & -\varepsilon_{x10} & Y_{10} + \delta_{y10} \\ -\varepsilon_{y10} & \varepsilon_{x10} & 1 & Z_{10} + \delta_{z10} \\ 0 & 0 & 0 & 1 \end{pmatrix}$$

HTMS FOR CAMERA 3

Compared to camera 1 and camera 2, the structural loop of camera 3 includes one more component, which is the roll. The structural loop for camera 3 is shown in Figure 18 and the corresponding analysis is listed in Table 4.

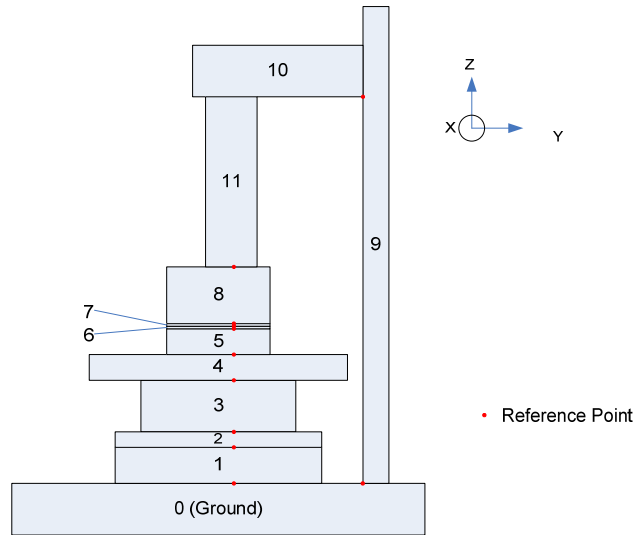


Figure 18: Structural loop for camera 3.

Table 4: Analysis of alignment errors for camera 3

Component	Motion	Offset	Positional error	Roll/Pitch/Yaw
0→1		Z_1 (44.65mm)		
1→2	x (314.17mm)	Z_2 (15.35mm)	δ_{x2}	Yaw: ε_{z2}
2→3		Z_3 (76.2mm)		
3→4		Z_4 (25.4mm)		
4→5		Z_5 (6.35mm)		Yaw: ε_{z5}
5→6		Z_6 (1mm)	δ_{z6}	
6→7		Z_7 (0.5mm)	$\delta_{x7}, \delta_{y7}, \delta_{z7}$	Yaw: ε_{z7}
7→8		Z_8 (66.5mm)	δ_{z8}	Yaw: ε_{z8}
0→9		Y_9 (106mm)		
9→10		Z_{10} (374.03mm)	δ_{x10} (6.31 μm) δ_{y10} (4.80 μm) δ_{z10} (12.44 μm) (due to thermal expansions)	
10→11		Y_{11} (-106mm) Z_{11} (-138.08mm)	δ_{x11} (1.48 μm) δ_{y11} (-3.47 μm) δ_{z11} (0.13 μm) (due to thermal expansions)	Yaw: ε_{x11} (-108.4 μrad) Yaw: ε_{y11} (-26.3 μrad)

The HTMs calculated for camera 3 are given below.

$$\begin{aligned}
 {}^0T_1 &= \begin{pmatrix} 1 & 0 & 0 & 0 \\ 0 & 1 & 0 & 0 \\ 0 & 0 & 1 & Z_1 \\ 0 & 0 & 0 & 1 \end{pmatrix} & {}^1T_2 &= \begin{pmatrix} 1 & -\varepsilon_{z2} & 0 & x + \delta_{x2} \\ \varepsilon_{z2} & 1 & 0 & 0 \\ 0 & 0 & 1 & Z_2 \\ 0 & 0 & 0 & 1 \end{pmatrix} \\
 {}^2T_3 &= \begin{pmatrix} 1 & 0 & 0 & 0 \\ 0 & 1 & 0 & 0 \\ 0 & 0 & 1 & Z_3 \\ 0 & 0 & 0 & 1 \end{pmatrix} & {}^3T_4 &= \begin{pmatrix} 1 & 0 & 0 & 0 \\ 0 & 1 & 0 & 0 \\ 0 & 0 & 1 & Z_4 \\ 0 & 0 & 0 & 1 \end{pmatrix} \\
 {}^4T_5 &= \begin{pmatrix} 1 & -\varepsilon_{z5} & 0 & 0 \\ \varepsilon_{z5} & 1 & 0 & 0 \\ 0 & 0 & 1 & Z_5 \\ 0 & 0 & 0 & 1 \end{pmatrix} & {}^5T_6 &= \begin{pmatrix} 1 & 0 & 0 & 0 \\ 0 & 1 & 0 & 0 \\ 0 & 0 & 1 & Z_6 + \delta_{z6} \\ 0 & 0 & 0 & 1 \end{pmatrix} \\
 {}^6T_7 &= \begin{pmatrix} 1 & -\varepsilon_{z7} & 0 & \delta_{x7} \\ \varepsilon_{z7} & 1 & 0 & \delta_{y7} \\ 0 & 0 & 1 & Z_7 + \delta_{z7} \\ 0 & 0 & 0 & 1 \end{pmatrix} & {}^7T_8 &= \begin{pmatrix} 1 & -\varepsilon_{z8} & 0 & 0 \\ \varepsilon_{z8} & 1 & 0 & 0 \\ 0 & 0 & 1 & Z_8 + \delta_{z8} \\ 0 & 0 & 0 & 1 \end{pmatrix} \\
 {}^8T_9 &= \begin{pmatrix} 1 & 0 & 0 & 0 \\ 0 & 1 & 0 & Y_9 \\ 0 & 0 & 1 & 0 \\ 0 & 0 & 0 & 1 \end{pmatrix} & {}^9T_{10} &= \begin{pmatrix} 1 & 0 & 0 & \delta_{x10} \\ 0 & 1 & 0 & \delta_{y10} \\ 0 & 0 & 1 & Z_{10} + \delta_{z10} \\ 0 & 0 & 0 & 1 \end{pmatrix} \\
 {}^{10}T_{11} &= \begin{pmatrix} 1 & 0 & \varepsilon_{y11} & \delta_{x11} \\ 0 & 1 & -\varepsilon_{x11} & Y_{11} + \delta_{y11} \\ -\varepsilon_{y11} & \varepsilon_{x11} & 1 & Z_{11} + \delta_{z11} \\ 0 & 0 & 0 & 1 \end{pmatrix}
 \end{aligned}$$

CALCULATED ERROR COMPONENTS

The linear and rotational error components in the HTM have to be used to obtain the positional error at the reference point. However, if the part is highly restricted, the error components can be replaced to zero for simplicity.

The values of the error components can be determined from accuracy data obtained from the data sheet of the equipments or materials for each of the components as well as experimental data measured with sufficient number of trials. The error components thus determined are used for the HTM analysis system. Errors, which are not mentioned below, are assumed negligibly small, therefore treated as zero, as previously mentioned.

It is assumed that the travel of the motor in general operation is 314.17 mm. From the experimentally measured data for the 404LXR linear motor, the static x and y-directional errors are 3.83 and 0.95 μm , respectively. Also for a 314.17 mm travel, a straight-line accuracy of 17 μm is expected; and hence the angle for the distortion is calculated as shown in equation (3).

$$\varepsilon_{z2} = \tan^{-1} \left(\frac{17 \times 10^{-3} \text{ mm}}{300 \text{ mm}} \right) \cong 3.247 \times 10^{-3} \text{ rad} \quad (3)$$

For the sample holder, since the sensitivity of the differential micrometer used for the measurement is 0.1 μm . Since the distance to the pivot bolt (pinhole) is 29.527mm, the angle of distortion due to the worst case of error on the micrometer is given by equation (4).

$$\varepsilon_{z5} = \tan^{-1} \left(\frac{0.1 \times 10^{-3} \text{ mm}}{29.5278 \text{ mm}} \right) \cong 1.940 \times 10^{-4} \text{ rad} \quad (4)$$

Assuming that the rubber is tightly stuck on the sample holder, there is no linear and rotational error in component 6. In other words, δ_{x6} , δ_{y6} and ε_{z6} are taken to be zero. The error on the sample substrate is obtained from the experimental measurements discussed in the previous sections. For Camera 1, δ_{x7} , δ_{y7} and ε_{z7} are 3.658 μm , 28.63 μm and 1.444rad, respectively. For Camera 2, the errors are 3.658 μm , 6.610 μm and 1.065rad, and for Camera 3, 21.33 μm , 8.085 μm and 0.362rad, respectively.

The equation of the change of length due to thermal expansion is based on the equation given by equation (5).

$$\Delta L = L\alpha \cdot \Delta T \quad (5)$$

However, since thermal expansion occurs in all three directions simultaneously, the error terms can be associated with all the six-degree of freedom. The numerical values for each component were obtained from the FEM analysis as explained in the previous section.

WORST CASE ERROR ESTIMATION

The error (x, y and z direction) calculated using HTMs for each points of interest in the camera system are summarized below in Table 5.

Table 5: Overall error due to camera system

Error	Camera 1	Camera 2	Camera 3
x(mm)	[0.01771]	[0.01798]	[0.03587]
y(mm)	[0.01440]	[-0.00218]	[-0.01782]
z(mm)	[-0.00765]	[-0.00873]	[-0.01257]

The overall accuracy for the system can be obtained by comparing the position of Camera 1 and Camera 2 with that of Camera 3. Therefore, individual error components for the x and y directions are listed in equations (6), (7) and (8).

$$\begin{aligned}\delta_{x13} &= \delta_{x1} + \delta_{x3} = 0.01771 + 0.01798 = \pm 0.03569 \\ \delta_{x23} &= \delta_{x2} + \delta_{x3} = 0.01798 + 0.03587 = \pm 0.05385\end{aligned}\quad (6)$$

$$\begin{aligned}\delta_{y13} &= \delta_{y1} + \delta_{y3} = 0.01440 + 0.01782 = \mp 0.03222 \\ \delta_{y23} &= \delta_{y2} + \delta_{y3} = 0.00218 + 0.01782 = \mp 0.02000\end{aligned}\quad (7)$$

$$\begin{aligned}\delta_{z13} &= \delta_{z1} + \delta_{z3} = 0.00765 + 0.01257 = \mp 0.02022 \\ \delta_{z23} &= \delta_{z2} + \delta_{z3} = 0.00873 + 0.01257 = \mp 0.02130\end{aligned}\quad (8)$$

Table 6: Summary of errors because of the camera system to the substrate

Camera	3 → 1	3 → 2
x	35.69 μm	53.85 μm
y	32.22 μm	20.00 μm
z	20.22 μm	21.30 μm

ERROR BUDGET

Table 1 gives the summary of the contribution of the different components of the system analyzed to the total error in the system. It can be seen that each component has a significant contribution to the total error in the system.

Table 7: Summary of contributions from different error sources

Error Source	Amplitude		
	x	y	z
Motor	~ 1 μm	~ 15 μm	0 μm
Clamp	~ 10 μm	~ 20 μm	0 μm
Thermal Expansion	~ 20 μm	~ 5 μm	~ 20 μm

DISCUSSION

As can be seen from Table 6, the errors calculated using the experimental values of substrate position error, and the effects of thermal expansion from finite element modeling are considerable, yet smaller than those errors measured experimentally. Qualitatively, the errors from thermal expansion were on the order of 20 μm , while δ_{x7} , δ_{y7} , the positional errors of the substrate were on the order of 30 μm , thus the calculated errors seem to be reasonable given our

assumptions. However, since measured alignment errors in practice on the order of $100\mu\text{m}$, we must assume that other sources of error play significant roles in the total error of the system. It is clear that improving positional errors from the substrate and improving the temperature control of the room can eliminate up to half of the error currently seen.

Some simple improvements to our model can perhaps point to other sources of error. For example, we did not consider the thermal expansion of the roll as part of our analysis. This could lead to an increase in all three components of error. We also have not calculated the stiffness of the Newport stages, which will cause motion during the acceleration of the substrate.

The thermal analysis of the system also shows that there is significant contribution from the thermal errors. This can be corrected by using a thermal compensation system, which can use the current temperature of the printing system as input. The compensation values can be pre-computed for the different temperature differences. These values can be then looked up from a table and used for the compensation while working with the system.

There may also be a series of procedural improvements that can be significant. For example, due to the confined space of the apparatus the cameras are constantly at a risk of being shifted (bumped) during operation, this may lead to offsets of camera position which cannot be easily modeled. An improved mounting brace could prevent this type of impact. Further, the temperature of the roll itself is subject to a variety of thermal changes, beyond those of the room, most importantly because the roll is subjected to an ultrasonic cleaning between each printing run. This may lead to temperature increases of up to 15°C . The use of a reference sample could help check or calibrate the camera position before each run, while the use of some thermocouple thermometers could either allow the alignment program to adjust for alignment offsets due to thermal variations or allow the operator to ensure the appropriate roll temperature is reached before it is used.

CONCLUSION

We have presented a new bench-top gravure printer intended for use as a research tool for printed electronics. Using a variety of techniques we have taken up the task of measuring the sources of alignment error for this machine, which was designed to achieve an alignment accuracy of $5\mu\text{m}$, but can currently only achieve $100\mu\text{m}$. We have found that a poor kinematic clamp design and poor thermal control can be accountable for up to half of this error. With the power of the models developed, we can develop a model for electronically compensating for thermal errors, and we can now easily include a number of other sources of error, in order to improve the total performance of the system.